

Journal of Materials Chemistry C

Accepted Manuscript



This is an *Accepted Manuscript*, which has been through the Royal Society of Chemistry peer review process and has been accepted for publication.

Accepted Manuscripts are published online shortly after acceptance, before technical editing, formatting and proof reading. Using this free service, authors can make their results available to the community, in citable form, before we publish the edited article. We will replace this *Accepted Manuscript* with the edited and formatted *Advance Article* as soon as it is available.

You can find more information about *Accepted Manuscripts* in the [Information for Authors](#).

Please note that technical editing may introduce minor changes to the text and/or graphics, which may alter content. The journal's standard [Terms & Conditions](#) and the [Ethical guidelines](#) still apply. In no event shall the Royal Society of Chemistry be held responsible for any errors or omissions in this *Accepted Manuscript* or any consequences arising from the use of any information it contains.

Crystal Structures and Optical Properties of New Quaternary Strontium Europium Aluminate Luminescent Nanoribbons

Cite this: DOI: 10.1039/x0xx00000x

Received 00th January 2012,
Accepted 00th January 2012

DOI: 10.1039/x0xx00000x

www.rsc.org/

Xufan Li,^{a,b,§} John D. Budai,^{*,c} Feng Liu,^{a,b} Yu-Sheng Chen,^d Jane Y. Howe,^{c,⊥}
Chengjun Sun,^e Jonathan Z. Tischler,^f Richard S. Meltzer^b and Zhengwei Pan^{*,a,b}

We report the synthesis and characterizations of three series of new quaternary strontium europium aluminate (Sr-Eu-Al-O; SEAO) luminescent nanoribbons that show blue, green, and yellow luminescence from localized Eu²⁺ luminescent centers. These three series of SEAO nanoribbons are: blue luminescent, tetragonal Sr_{1-x}Eu_xAl₆O₁₀ (0 < x < 1) (*b*-SEAO), green luminescent, monoclinic Sr_{1-x}Eu_xAl₂O₄ (0 < x < 1) (*g*-SEAO), and yellow luminescent, hexagonal Sr_{1-x}Eu_xAl₂O₄ (0 < x < 1) (*y*-SEAO). Among these three series of SEAO nanoribbons, the *b*-SEAOs and *y*-SEAOs are new compounds that have not been reported before. The crystal structures of the SEAO nanoribbons were comprehensively studied using various synchrotron X-ray diffraction techniques and the effects of crystal structures on materials' luminescence properties were investigated. These one-dimensional SEAO luminescent nanoribbons can function as both light generators and waveguides, and thus have promising potential as the building blocks in miniaturized photonic circuitry.

Introduction

Highly-integrated photonics possess advantages over silicon-based electronics because of their higher speed and lower power dissipation, which are of great significance to the development of advanced computing, communication, and other information processing devices.¹⁻⁴ One potential route to realize integrated photonics is the assembly of photonic circuitry from nanowire- or nanoribbon-based components that assume different optical functions (e.g., light generation, routing, and detection).^{5,6} In the past decade, an array of nanowire/nanoribbon-based devices, which can be potentially used as functional elements for photonic circuitry, have been fabricated, including waveguides,^{5,6} lasers,⁷⁻⁹ light-emitting diodes (LEDs),¹⁰⁻¹² photodetectors,¹³ and non-linear optical converters.¹⁴ Among these devices, waveguides are essential to photonic circuitry because of their capabilities in capturing photons generated by light sources (e.g., lasers and LEDs) and transporting them to other functional components such as photodetectors and converters.^{1,2,5,15}

The first 'proof-of-concept' miniaturized photonic circuitry was constructed from ZnO (or GaN) nanowires and SnO₂ nanoribbons, which marks the first step toward highly-integrated photonic systems.^{4,5} In such a miniaturized photonic circuitry, SnO₂ nanoribbons (~100–400 nm in width) function as an effective waveguide which can guide either visible photoluminescence or the emission from the ZnO (or GaN) nanowire light sources through optical coupling. However, these materials suffer two critical constraints in their optical performance. First, the emissions, either

from a light source (e.g., green light peaking at ~520 nm from ZnO nanowires) or from a SnO₂ nanoribbon waveguide (green light peaking at ~500 nm or orange light peaking at ~590 nm), are related to crystal defects introduced during synthesis.¹⁶⁻¹⁸ This means that the nanowires and nanoribbons synthesized in different batches may show inconsistent optical performances (e.g., different kinds of defects may be introduced, causing variation in emission wavelength). Second, the limited emission colors (green and orange) from ZnO (or GaN) nanowires/SnO₂ nanoribbons prevent them from producing all the necessary photonic components in the visible spectral region. To overcome these constraints, new types of luminescent nanowires/nanoribbons that can function as both light generators emitting characteristic light with diverse colors and waveguides for effective light propagation are highly desired.

Rare-earth (RE)-activated phosphors, whose luminescence is usually determined by the nature of the RE luminescent centers,¹⁹ are the most important family of luminescent materials. Among the RE ions, divalent europium (Eu²⁺) is receiving increased attention for its remarkable optical performance in solids including the characteristic band-shape emissions (generally attributed to inter-configurational 4f⁶5d → 4f⁷ transitions) that can be tuned from near-ultraviolet (UV) to deep red and the broad excitation that can be extended from the visible to X-ray regions in different hosts.²⁰⁻²³ Tunable emission covering the entire visible region is desirable for full-spectrum photonic systems,¹⁵ and the broad excitation is highly advantageous because it enables the materials to be excited by various excitation sources. These favorable luminescence properties

suggest that if Eu^{2+} -activated luminescent materials can be fabricated into one-dimensional nanowires or nanoribbons, they will provide a broad range of high-quality, nanoscale luminescent building blocks for fabricating photonic circuits with enhanced functionalities.

Recently, our laboratory synthesized three kinds of Eu^{2+} -activated ternary europium aluminate (Eu-Al-O , called EAO hereafter) nanoribbons by using a modified carbothermal reaction and vapor-phase deposition method.²⁴ These three EAOs are blue luminescent $\text{EuAl}_6\text{O}_{10}$ (*b*-EAO) with a new composition and a new tetragonal lattice structure, green luminescent EuAl_2O_4 (*g*-EAO) with a monoclinic lattice structure, and orange luminescent EuAl_2O_4 (*o*-EAO) with a new hexagonal lattice structure. In this article, we show that the Eu ions in each of these three ternary EAOs can be substituted by Sr ions over the full composition range (owing to the great similarity in radius of Eu and Sr ions),²⁵ leading to the formation of three series of new quaternary strontium europium aluminate (Sr-Eu-Al-O , called SEAO hereafter) nanoribbons. These three series of quaternary SEAO nanoribbons are blue luminescent, tetragonal $\text{Sr}_{1-x}\text{Eu}_x\text{Al}_6\text{O}_{10}$ ($0 < x < 1$), green luminescent, monoclinic $\text{Sr}_{1-x}\text{Eu}_x\text{Al}_2\text{O}_4$ ($0 < x < 1$), and yellow luminescent, hexagonal $\text{Sr}_{1-x}\text{Eu}_x\text{Al}_2\text{O}_4$ ($0 < x < 1$). Compared with their respective EAO counterparts, the three SEAOs exhibit more complicated microstructures and remarkably, the yellow luminescent SEAO exhibits tunable emission colors from green-yellow to orange-yellow depending on Eu concentration. The successful synthesis of these three series of SEAO nanoribbons greatly enriches the new family of Eu^{2+} -activated luminescent nanowires or nanoribbons, and thus provides more building blocks for miniaturized photonic circuitry. In this article, we perform comprehensive structural and optical characterizations on these three series of SEAO nanoribbons.

Experimental

Materials synthesis

The SEAO nanoribbons were synthesized through a carbothermal reaction and vapor-phase deposition method in a strictly controlled tube furnace system (Supporting Figure S1a). High-purity SrO (99.99%), Eu_2O_3 (99.99%) and Al_2O_3 (99.99%) powders were mixed and ground with graphite powder (99.99%) at certain molar ratios (see Results and Discussion). The functions of the graphite powder are to reduce the oxides and to create a weakly reducing environment for the formation of divalent europium. Ultrahigh-purity argon (99.999%) was used as the carrier gas. Alumina (purity, 99.8%) plates were used as the substrates for material deposition and growth.

In a typical run, ~ 1 g of source powder was loaded into an alumina boat. The boat was then placed at the center of an alumina tube that was inserted into a horizontal tube furnace. An alumina substrate (~ 6 cm long, 2.5 cm wide and 0.5 cm thick) was placed at the growth region about 10 cm downstream of the source. After evacuating the alumina tube to $\sim 2 \times 10^{-3}$ Torr, the source powder was heated to 1450 °C (with a ramping rate of 15 °C/min) under a flowing argon atmosphere at a flow rate of 50 sccm (standard cubic centimeter per minute) and a pressure of 5–10 Torr. The vapor-phase

reactants generated by the carbothermal reaction were transported by the flowing argon gas to the growth region, where the temperature undergoes a gradient from ~ 1400 to ~ 1000 °C, to feed the growth of SEAO nanoribbons. The reaction typically lasted for 2 h. After reaction, the furnace was cooled down naturally to room temperature.

Characterizations

The as-synthesized products were initially examined using an optical microscope with the samples being excited by a 365 nm UV lamp. The morphology and microstructure were characterized and analyzed using a scanning electron microscope (SEM; FEI Inspect F FEG-SEM) and a transmission electron microscope (TEM; Hitachi HF-3300 FEG STEM/TEM). The composition was analyzed using both an energy-dispersive X-ray spectroscopy (EDS) attached to the TEM and an inductively coupled plasma-mass spectrometer (ICP-MS, VG PlasmQuad 3).²⁶ For ICP-MS measurements, ~ 1 mg sample was dissolved in a 10 ml, 2% HNO_3 solution, which was then diluted by 200 times.

The valence state of the Eu ions was measured using X-ray absorption near edge structure (XANES) spectroscopy on the Eu L_{3-} edge. The measurement was carried out at room temperature using linearly polarized X-ray at the Advanced Photon Source (APS) beamline 20-BM-B.²⁷ A multi-element Ge detector was used to select the Eu fluorescence for counting.

The crystal structures were investigated using a combination of powder X-ray diffraction (XRD) and synchrotron X-ray microdiffraction techniques. The powder XRD measurements were carried out using both conventional X-ray source (PANalytical X'Pert PRO Diffractometer with $\text{Cu K}\alpha$ radiation, $\lambda = 1.5406$ Å) and monochromatic synchrotron radiation ($\lambda = 0.4131$ Å) at the APS beamline 11-BM-B.²⁸ For the synchrotron XRD measurements, the SEAO nanoribbons were encapsulated inside a narrow capillary tube (~ 2 mm in diameter). The diffraction patterns were fit by JADE diffraction analysis software (Materials Data, Inc) to determine the lattice parameters and to identify any known phases.

The X-ray microdiffraction measurements from individual SEAO nanoribbons were carried out using both monochromatic and polychromatic synchrotron radiation. Monochromatic (at 28 keV) microdiffraction using rotation crystallography at the APS 15-ID ChemMatCARS facility (Bruker APEX2 software) revealed the crystallographic information of individual nanoribbons including the atomic positions and real symmetry of unit cells. The diameter of the X-ray beam was ~ 100 μm . Polychromatic (~ 6 –28 keV) Laue microdiffraction carried out at the APS beamline 34-ID-E^{29–32} revealed the local lattice structures including the lattice orientations and weak superstructure ordering. At this facility, a pair of elliptically curved Kirkpatrick-Baez reflecting mirrors was used to focus a synchrotron X-ray beam onto a nanoribbon mounted on a copper TEM grid. The focused beam diameter was ~ 0.5 μm . Scattering of the microbeam generated a Laue diffraction pattern that was collected using a Perkin-Elmer large area amorphous silicon detector. A double-crystal Si monochromator was inserted into the incident X-ray beam for energy scans in order to obtain absolute lattice parameters. The Laue diffraction patterns were analyzed using Igor Pro software (WaveMetrics Inc.) developed at the beamline. A

high-resolution television camera was used to optically image the ribbon under investigation. The optical luminescence generated due to X-ray microbeam excitation was also collected by a fiber-optic coupled optical spectrometer (Ocean Optics CHEMUSB4-VIS-Fiber Spectrophotometer).

The photoluminescence (PL) emission and excitation spectra were measured at both room temperature and 77 K using a Horiba Fluorolog3-2iHR320 spectrofluorometer equipped with a 450 W xenon lamp as the excitation source. For the measurements at 77 K, the samples were mounted on a copper sample holder that was cooled in a quartz cryostat filled with liquid nitrogen.

The PL emission decay curves were measured under 355 nm excitation of a pulsed Nd:YAG laser. The monitored emission wavelength was spectrally separated by a monochromator and detected using a digital oscilloscope connected to a cooled photomultiplier tube. The luminescence quantum efficiency was measured using a quantum yield accessory attached to the spectrofluorometer.

Results and Discussion

Synthesis of whisker-like blue, green and yellow luminescent SEAO phosphors

The synthesis of the SEAO phosphors is sensitive to the growth parameters, especially the growth temperature and the molar ratios of the source oxides. By adjusting the growth conditions, we were able to synthesize three types of SEAO products with luminescence colors of blue, green, and yellow. Figure 1a shows an optical micrograph of the yellow and green luminescent products (under the excitation of a 365 nm UV lamp) obtained at SrO/Eu₂O₃/Al₂O₃/graphite molar ratio of ~1/0.05/0.1/6, reaction chamber pressure of 5 Torr, argon gas flow rate of 50 sccm, and growth time of 2 h. The luminescent products were formed in a 6-cm-long region covering temperature from ~1350 to ~1000 °C, with the yellow luminescent product depositing in the high-temperature region (~1350–1200 °C) and the green luminescent product forming in the low-temperature region (~1200–1000 °C) (see also Figure S1). When more Al₂O₃ powder was added to the source, e.g., the SrO/Eu₂O₃/Al₂O₃/graphite molar ratio was changed to ~1/0.05/0.3/6, and the chamber pressure was increased to 10 Torr (the other synthesis parameters were kept unchanged), the growth of the yellow and green luminescent products was completely suppressed; instead, a blue luminescent product (under the illumination of a 365 nm UV lamp) was obtained in the entire growth region from ~1350 to ~1050 °C (Figure 1b and Figure S1). Observations using an optical microscope revealed that all the three luminescent products are whisker-like and each whisker emits uniform luminescence along its entire length when illuminated by a 365 nm UV lamp, as shown in the optical micrographs in Figure 1c–e.

Our synthesis experiments also showed that decreasing the Eu₂O₃ content in the source (with other synthesis parameters remaining unchanged) did not change the luminescence colors of the blue and green luminescent products, but caused a slight change in emission colors for the yellow luminescent products.

For example, when the SrO/Eu₂O₃ molar ratio decreased from ~1/0.05 to ~1/0.005, and to ~1/0.0005, the emission color of the yellow luminescent products changed from orange-yellow (Figure 1e) to bright yellow (Figure 1f), and to green-yellow (Figure 1g).

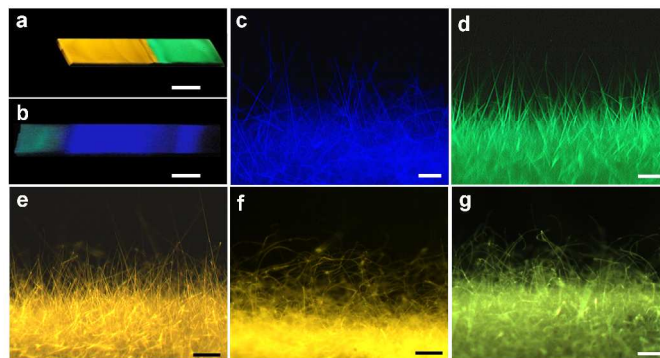


Figure 1. (a–e) Optical micrographs of blue, green, and orange-yellow luminescent SEAO nanoribbons synthesized at SrO/Eu₂O₃ molar ratio of ~1/0.05. (f, g) Optical micrographs of yellow and green-yellow luminescent SEAO nanoribbons synthesized at SrO/Eu₂O₃ molar ratio of 1/0.005 and 1/0.0005, respectively. Micrographs (a–b) were taken by a digital camera, while micrographs (c–g) were taken by a digital optical microscope. All micrographs were taken with the samples being illuminated by a 365 nm UV lamp. Scale bars: 1 cm for (a,b) and 200 μm for (c–g).

Morphology and compositions of SEAO nanoribbons

Figures 2a–c show SEM images of the blue, green, and yellow luminescent whiskers synthesized with a SrO/Eu₂O₃/Al₂O₃/graphite molar ratio of ~1/0.05/0.1/6. The whiskers have typical lengths in the range of several tens to several hundreds of micrometers. TEM observations (Figures 2d–f) reveal that the geometrical shape of the whisker-like products is actually a ribbon with a rectangular cross section. Each ribbon typically has a uniform width and thickness along its entire length, and the typical widths and thicknesses of the ribbons are in the range of 0.2–1.5 μm and 50–300 nm, respectively. Composition analyses using an EDS attached to the TEM reveal that the nanoribbons are composed of Sr, Eu, Al, and O (Figures 2g–i), and each element is uniformly distributed across the ribbons, as determined by EDS elemental line scan in the scanning STEM mode (insets of Figures 2g–i).

Quantitative composition analyses using EDS and ICP-MS consistently show that the (Sr+Eu)/Al atomic ratio in the blue luminescent ribbons is ~1/6, while the ratios in the green and yellow luminescent ribbons are approximately the same, which are ~1/2. The Eu concentration in the three types of luminescent products was able to be tuned between 0 and 100% by adjusting the SrO/Eu₂O₃ molar ratios in the source materials. For example, when the SrO/Eu₂O₃ molar ratios are 1/0.05, 1/0.005, and 1/0.0005, the average Sr/Eu atomic ratios in the resulting three luminescent products are ~8/1 (i.e., ~11% Eu), ~40/1 (i.e., ~2.5% Eu), and ~250/1 (i.e., ~0.4% Eu), respectively, as precisely determined by the ICP-MS analyses. XANES measurements on the Eu L₃ edge (Figure S2) revealed that the Eu ions in the three luminescent products are

all in the divalent state, i.e., Eu^{2+} . This composition information, together with the fact that Sr^{2+} and Eu^{2+} ions can be freely substituted in aluminate lattices, enables us to determine the chemical formulas of the three series of strontium europium aluminates as $\text{Sr}_{1-x}\text{Eu}_x\text{Al}_6\text{O}_{10}$ ($0 < x < 1$) for the blue luminescent

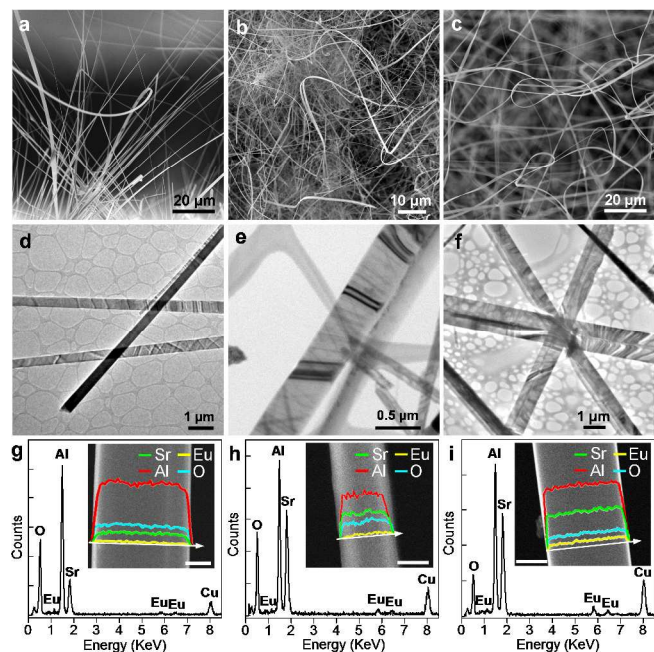


Figure 2. (a–c) SEM images of blue, green, and orange-yellow luminescent $\text{SE}_{0.11}\text{AO}$ nanoribbons. (d–f) TEM images of blue, green, and orange-yellow luminescent $\text{SE}_{0.11}\text{AO}$ nanoribbons. (g–i) EDS spectra of blue, green, and orange-yellow luminescent $\text{SE}_{0.11}\text{AO}$ nanoribbons acquired in a TEM. Insets are EDS elemental line scan along the transverse direction of individual ribbons acquired under the STEM mode in a TEM. Scale bars for the insets: 100 nm.

aluminates (called *b*-SEAO), $\text{Sr}_{1-x}\text{Eu}_x\text{Al}_2\text{O}_4$ ($0 < x < 1$) for the green luminescent aluminates (called *g*-SEAO), and also $\text{Sr}_{1-x}\text{Eu}_x\text{Al}_2\text{O}_4$ ($0 < x < 1$) for the yellow luminescent aluminates (called *y*-SEAO). When $x = 1$, the three SEAO formulas become $\text{EuAl}_6\text{O}_{10}$, EuAl_2O_4 , and EuAl_2O_4 , which correspond to the formulas of the three EAOs, i.e., *b*-EAO, *g*-EAO, and *o*-EAO, respectively.²⁴ This means that the three EAOs can be regarded as the extreme cases of the three SEAOs. Indeed, besides the luminescence colors and compositions, as will be discussed below, the SEAOs share similar crystal structures and luminescence performances to their respective EAO counterparts. Among the three SEAOs, the blue luminescent $\text{Sr}_{1-x}\text{Eu}_x\text{Al}_6\text{O}_{10}$ ($0 < x < 1$) are new compositions which have not been reported before. The green luminescent $\text{Sr}_{1-x}\text{Eu}_x\text{Al}_2\text{O}_4$ ($0 < x < 1$) are similar to a reported green $\text{SrAl}_2\text{O}_4:\text{Eu}^{2+}$ phosphor,^{33,34} which was synthesized in the form of powders through solid-state reaction,³⁴ sol-gel route,³⁵ or by combustion method.³⁶ The yellow luminescent $\text{Sr}_{1-x}\text{Eu}_x\text{Al}_2\text{O}_4$ ($0 < x < 1$) have the same composition as the *g*-SEAOs; however, their completely different luminescent colors are due to the fact (see below) that they are two different compounds having different crystal structures. Hence, the *y*-SEAOs are also new compounds.

To simplify the discussion, in the following sections we focus on the nanoribbons synthesized at $\text{SrO}/\text{Eu}_2\text{O}_3$ ratios of 1/0.0005, 1/0.005, and 1/0.05, which produced nanoribbons with average Sr/Eu atomic ratios being $\sim 8/1$ (i.e., $\sim 11\%$ Eu), $\sim 40/1$ (i.e., $\sim 2.5\%$ Eu), and $\sim 250/1$ (i.e., $\sim 0.4\%$ Eu), respectively. Specifically, we focus our discussions on blue luminescent $\text{Sr}_{1-x}\text{Eu}_x\text{Al}_6\text{O}_{10}$, green luminescent $\text{Sr}_{1-x}\text{Eu}_x\text{Al}_2\text{O}_4$, and yellow luminescent $\text{Sr}_{1-x}\text{Eu}_x\text{Al}_2\text{O}_4$ nanoribbons with $x = 0.004$, 0.025, and 0.11, which are called *b*-, *g*- and *y*- $\text{SE}_{0.004}\text{AO}$, *b*-, *g*- and *y*- $\text{SE}_{0.025}\text{AO}$, and *b*-, *g*- and *y*- $\text{SE}_{0.11}\text{AO}$, respectively. In addition, in the following discussion, SEAOs refer to all the strontium europium aluminates, and *b*-SEAO, *g*-SEAO, and *y*-SEAO refer to the groups of strontium europium aluminates with luminescent colors of blue, green, and yellow, respectively.

Crystal structures of SEAO nanoribbons determined by powder XRD techniques

The crystal structures of the three series of SEAO nanoribbons were initially studied using conventional powder XRD ($\lambda = 1.5406$ Å). Figures 3a–c show the conventional powder XRD patterns of *b*- $\text{SE}_{0.11}\text{AO}$, *g*- $\text{SE}_{0.11}\text{AO}$ and *y*- $\text{SE}_{0.11}\text{AO}$ nanoribbons. By searching the ICDD (International Centre for Diffraction Data) database, the XRD pattern of *g*- $\text{SE}_{0.11}\text{AO}$ (Figure 3b) matches monoclinic SrAl_2O_4 with lattice parameters of $a = 8.447$ Å, $b = 8.816$ Å, $c = 5.163$ Å and $\beta = 93.42^\circ$ (JCPDS No. 74–0794), indicating that the *g*- $\text{SE}_{0.11}\text{AO}$ has the same lattice structure as the reported green $\text{SrAl}_2\text{O}_4:\text{Eu}^{2+}$ phosphor.^{36,37} For the *b*- $\text{SE}_{0.11}\text{AO}$ (Figure 3a) and *y*- $\text{SE}_{0.11}\text{AO}$ (Figure 3c), however, no corresponding phases or isostructural phases are available in the ICDD database or other commonly available databases such as the Inorganic Crystal Structure Database. XRD measurements on $\text{SE}_{0.004}\text{AO}$ s and $\text{SE}_{0.025}\text{AO}$ s reveal almost the identical patterns as their $\text{SE}_{0.11}\text{AO}$ counterparts (Figure S3). By comparing the patterns of the SEAOs with those of the EAOs, we found that the patterns of the SEAOs are essentially the same as those of their EAO counterparts (Figure S3).²⁴ These results indicate that the crystal structures of the three series of SEAOs are largely independent of the Eu concentrations and are isostructural to the three EAOs. Therefore, like *b*-EAO and *o*-EAO, the *b*-SEAOs and *y*-SEAOs have a new tetragonal structure and a new hexagonal structure, respectively. Since the crystal structures of each series of SEAOs are largely independent of Eu concentration, below we use *b*- $\text{SE}_{0.11}\text{AO}$ and *y*- $\text{SE}_{0.11}\text{AO}$ nanoribbons as examples for *b*-SEAOs and *y*-SEAOs, respectively, in detailed crystal structure studies.

The crystal structures of *b*-SEAO and *y*-SEAO nanoribbons were further measured using high-resolution synchrotron powder XRD ($\lambda = 0.4131$ Å; at 30.0 keV) at the APS beamline 11-BM-B. Figures 4a and 4b show the high-resolution synchrotron powder XRD patterns of *b*- $\text{SE}_{0.11}\text{AO}$ and *y*- $\text{SE}_{0.11}\text{AO}$ nanoribbons, respectively, which are consistent with the conventional XRD patterns shown in Figures 3a and 3c, respectively. By using JADE diffraction analysis software, we are able to identify the crystal symmetries and determine the lattice parameters that best match the diffraction patterns. The analyses show that the structure of *b*- $\text{SE}_{0.11}\text{AO}$ can be described as a new tetragonal phase with lattice parameters of $a = b =$

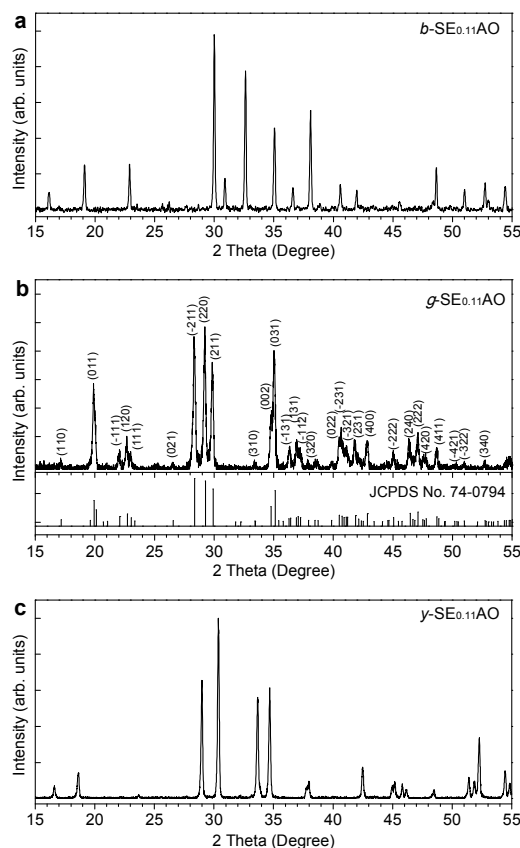


Figure 3. Conventional powder XRD patterns recorded on (a) b -SE_{0.11}AO, (b) g -SE_{0.11}AO, and (c) γ -SE_{0.11}AO nanoribbons with Cu K α_1 radiation ($\lambda = 1.5406 \text{ \AA}$). The tick marks below the XRD pattern of g -SE_{0.11}AO in (b) indicate the diffraction peak positions of monoclinic SrAl₂O₄ according to JCPDS #74-0794.

7.754 \AA and $c = 5.803 \text{ \AA}$ (detailed fitting information by JADE analysis is given in Table S1). Compared with its EAO counterpart,²⁴ the b -SE_{0.11}AO exhibits a smaller tetragonal unit cell than the b -EAO ($a = b = 7.77 \text{ \AA}$ and $c = 17.30 \text{ \AA}$) with very close a and b lengths but approximately one-third of c length. The synchrotron powder XRD pattern of γ -SE_{0.11}AO can be best indexed as a new hexagonal phase with lattice parameters of $a = b = 6.155 \text{ \AA}$ and $c = 10.58 \text{ \AA}$ (detailed fitting information by JADE analysis is given in Table S2), which are almost the same as the o -EAO ($a = b = 6.15 \text{ \AA}$ and $c = 10.57 \text{ \AA}$).²⁴

Structural analyses using Laue microdiffraction technique

Besides the XRD measurements on bulk nanoribbon samples, we also carried out spatially-resolved Laue microdiffraction measurements on individual nanoribbons using polychromatic (~ 6 – 28 keV) synchrotron X-ray microbeam at the APS beamline 34-ID-E to get more detailed structural information, because this technique can reveal weak scattering effects such as superstructure reflections. Figure 5a shows an optical micrograph of several b -SE_{0.11}AO nanoribbons mounted on a copper grid for Laue microdiffraction measurements. A focused polychromatic X-ray microbeam (diameter $\sim 0.5 \mu\text{m}$) strikes ribbon R1 at the beam

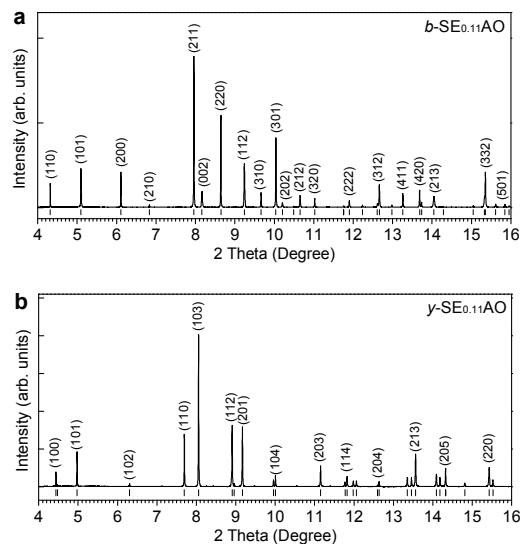


Figure 4. Synchrotron powder XRD pattern of (a) b -SE_{0.11}AO and (b) γ -SE_{0.11}AO nanoribbons using a monochromatic X-ray beam ($\lambda = 0.4131 \text{ \AA}$). The tick marks below each pattern indicate the peak positions identified by JADE software. Detailed fitting information is shown in Supporting Table S1 and Table S2.

position circled. Scattering of the X-ray microbeam by the ribbon generates a Laue diffraction pattern (Figure 5b) containing hundreds of sharp diffraction peaks from crystal planes in different orientations. The sharp peaks reveal good crystal quality of the ribbon. The Laue patterns typically do not change as the sample is translated, showing that individual ribbons are generally single crystals along their full length. Using the analysis software, most of the diffraction peaks in Figure 5b can be indexed using a tetragonal unit cell with lattice parameters of $a = b = 7.76 \text{ \AA}$ and $c = 5.77 \text{ \AA}$ (Figure 5c), which is consistent with the results from powder diffraction (Figure 4a). However, a small fraction of peaks remain unindexed using such a tetragonal unit cell, and these unindexed peaks are generally weaker and more diffuse than the indexed ones, as the top line of peaks enclosed by a dashed square and redisplayed as the inset in Figure 5c. These unindexed peaks are associated with a superstructure modulation. Indeed, by elongating the original tetragonal c length by three times (i.e., by using tetragonal lattice parameters of $a = b = 7.76 \text{ \AA}$ and $c = 17.31 \text{ \AA}$; the same as b -EAO), we are able to index all the diffraction peaks in the Laue diffraction pattern, as shown in Figure 5d. The above indexations indicate that the lattice structure of b -SE_{0.11}AO can be described as a fundamental tetragonal unit cell with lattice parameters of $a = b = 7.76 \text{ \AA}$ and $c = 5.77 \text{ \AA}$ plus a superstructure with the same a and b lengths but a tripled c length. However, close observation of the indexed pattern in Figure 5d reveals that the sharp diffraction peaks from the smaller, fundamental tetragonal unit cell accurately locate at the calculated angular positions, but the weaker and more diffuse peaks related to the superstructure slightly shift from the calculated positions, as shown in the enlarged pattern in Figure 5e. This means that the superstructure is actually not a commensurate periodic tripling of the fundamental unit cell along the c axis, but rather associated with a slightly incommensurate modulation that includes some local

fluctuations in periodicity.³⁸ Such superstructure ordering was observed in all of the measured tetragonal b -SE_{0.11}AO nanoribbons. It should be noted that the superstructure ordering in b -SE_{0.11}AO is weak, since no diffraction peaks associated with this incommensurate superstructure were observed in the powder XRD pattern from b -SE_{0.11}AO in Figure 4a.

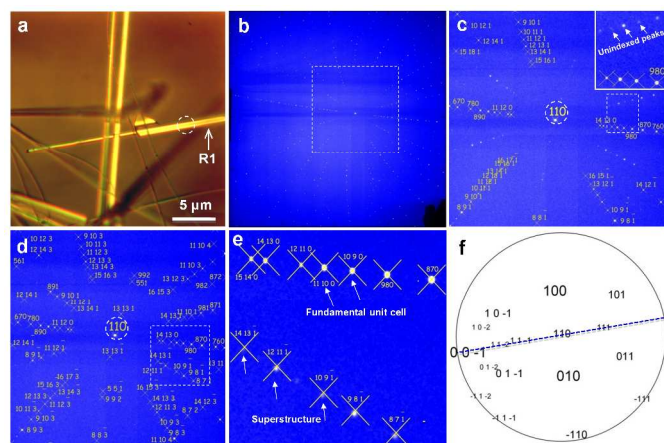


Figure 5. (a) Bright-field optical micrograph of b -SE_{0.11}AO nanoribbons mounted on a copper grid for polychromatic synchrotron X-ray Laue microdiffraction measurements. The dashed-line circle indicates the position where the focused X-ray microbeam (~ 0.5 μm in diameter) strikes ribbon R1. (b) Laue diffraction pattern acquired from ribbon R1 in (a). (c) Enlarged Laue diffraction pattern of the dashed-line square area in (b). The pattern is indexed using a tetragonal unit cell with lattice parameters of $a = b = 7.76$ \AA and $c = 5.77$ \AA . The (110) reflection is circled. Inset is the enlarged view of the dashed-line square area in (c). (d) Enlarged Laue diffraction pattern of the dashed-line square area in (b). The pattern is indexed using a tetragonal unit cell with lattice parameters of $a = b = 7.76$ \AA and $c = 17.31$ \AA . The (110) reflection is circled. (e) Enlarged Laue diffraction pattern of the dashed-line square area in (d). The crosses indicate the calculated peak positions using the tetragonal unit cell with lattice parameters of $a = b = 7.76$ \AA and $c = 17.31$ \AA . (f) Stereographic projection created from the indexed Laue diffraction pattern in (d), showing that ribbon R1 grows along [001] direction.

Based on the indexed fundamental Laue diffraction pattern in Figure 5c, a stereographic projection is generated for the b -SE_{0.11}AO ribbon R1, as shown in Figure 5f. From this projection, the crystal orientation of the tetragonal ribbon can be described as (110) surface planes with [001] direction along the long axis of the ribbon. This orientation was consistently observed in most of the measured tetragonal b -SE_{0.11}AO nanoribbons.

Figure 6a shows a γ -SE_{0.11}AO nanoribbon mounted on a copper grid and Figure 6b shows the polychromatic Laue microdiffraction pattern acquired from this ribbon. The pattern contains both diffraction peaks and streaks that consistently appear between the peaks (indicated by blue arrows in Figure 6c). The peaks are sharp, revealing good crystal periodicity of an average lattice structure in the γ -SE_{0.11}AO ribbon, and can be accurately indexed using a hexagonal unit cell with lattice

parameters of $a = b = 6.16$ \AA and $c = 10.57$ \AA (Figure 6c). The streaks between the peaks, including a continuous line of intensity through the ($hk0$) reflections as indicated by a red arrow in Figure 6c, suggest the existence of a superstructure with significant local planar disorder. The extra diffraction streaks can be indexed approximately using hexagonal lattice parameters of $a = b = 18.48$ (i.e., 3×6.16) \AA and $c = 10.57$ \AA (Figure 6d), indicating that the short-range superstructure

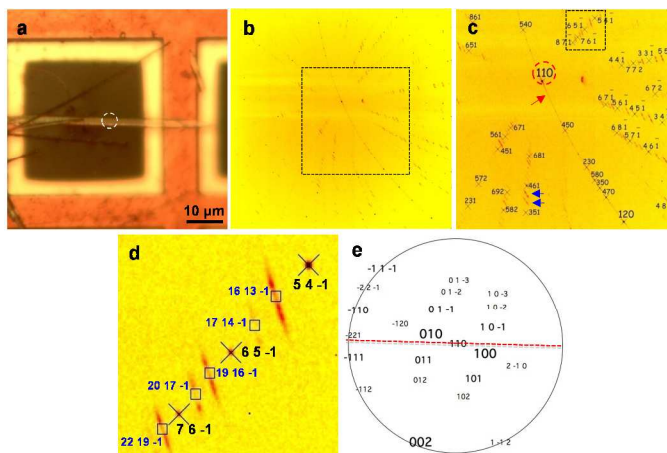


Figure 6. (a) Bright-field optical micrograph of a γ -SE_{0.11}AO nanoribbon mounted on a copper grid for Laue microdiffraction measurements. The dashed-line circle indicates the position where the focused X-ray microbeam (~ 0.5 μm in diameter) hits the ribbon. (b) Laue diffraction pattern acquired from the ribbon in (a). (c) Enlarged Laue diffraction pattern of the dashed-line square area in (b). The pattern is indexed using hexagonal lattice parameters of $a = b = 6.16$ \AA and $c = 10.57$ \AA . The (110) reflection is circled. (d) Enlarged Laue diffraction pattern of the dashed-line square area in (c). The crosses indicate the calculated angular positions of the hexagonal crystal with lattice parameters of $a = b = 6.16$ \AA and $c = 10.57$ \AA . The squares indicate the calculated angular positions of a hexagonal unit cell with lattice parameters of $a = b = 18.48$ \AA and $c = 10.57$ \AA . (e) Stereographic projection created from the indexed Laue diffraction pattern in (c), showing that ribbon grows along $[-221]$ direction.

shows approximately tripling in the a - b plane. It is worth noting here that the tripling is an approximation. This is because, as is clearly shown in Figure 6d, the streaks are split into two lobes of intensity away from the center (i.e., the zone axis). In addition, the centers of the streaks are often observed as shifted slightly from the calculated positions, meaning that the superstructure is not exactly along the [110] direction and is incommensurate. The stereographic projection (Figure 6e) generated from the indexed Laue pattern (Figure 6c) shows that the orientation of the hexagonal γ -SE_{0.11}AO ribbon in Figure 6a can be described as (110) surface planes with $\{-221\}$ plane-normal along the long growth axis. Among all the measured γ -SE_{0.11}AO ribbons, most of them show the similar short-range, incommensurate superstructure order and the same crystal orientation as the ribbon in Figure 6a.

Crystallographic analyses using monochromatic X-ray microdiffraction technique

The above characterizations using powder XRD and polychromatic synchrotron Laue microdiffraction determined the phases and lattice parameters of *b*-SEAO and γ -SEAO nanocrystals, but did not yield atomic coordinates inside the unit cell. Determining the local atomic arrangements inside the unit cell is important for understanding the origins of physical properties including luminescence. Thus, the crystallographic information describing the SEAO nanoribbons, including the atomic positions and real

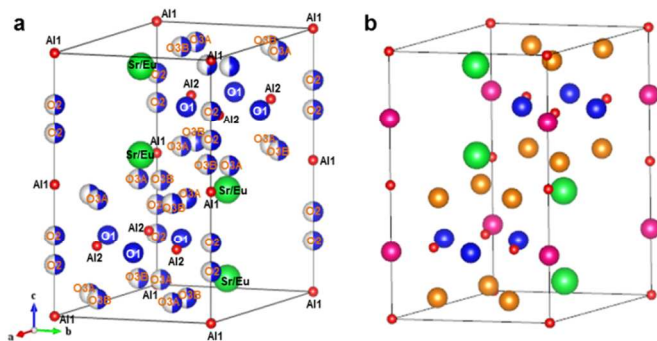


Figure 7. (a) Unit cell of γ -SE_{0.11}AO nanoribbon determined by synchrotron monochromatic microdiffraction. Green balls: Sr/Eu atoms, red balls: Al atoms, blue balls: O atoms at O1 sites, blue-white double color balls: O atoms at O2, O3A, and O3B sites. (b) Simplified unit cell of γ -SE_{0.11}AO. Pink balls: O atoms at halfway position of O2 pair in (a), orange balls: O atoms at halfway position of O3A–O3B pair in (a). Detailed atomic positions are given in Supporting Table S3.

symmetry of unit cells, was further studied using monochromatic X-ray microdiffraction at the APS 15-ID ChemMatCARS facility. Figure 7 shows the average unit cell of γ -SE_{0.11}AO determined by the crystallographic analysis and Table S3 shows the atomic coordinates corresponding to an R-factor least squares fit of less than 0.05. The average unit cell structure and the atomic coordinates of *b*-SE_{0.11}AO are given in Figure S4 and Table S4, respectively. Below we focus our discussion on the crystallographic results obtained from γ -SE_{0.11}AO; the results obtained from *b*-SE_{0.11}AO are briefly discussed in Figure S4.

The crystallographic analyses reveal that the γ -SE_{0.11}AO nanoribbons has a hexagonal space lattice (trigonal point group *P*-31*c*, #163 in International Tables for Crystallography) with a set of lattice parameters of $a = b = 6.146 \text{ \AA}$, $c = 10.559 \text{ \AA}$, $\alpha = \beta = 90^\circ$ and $\gamma = 120^\circ$, which is consistent with the results from powder diffraction and Laue microdiffraction. As shown in Figure 7a, the unit cell contains fully occupied 4 Sr/Eu sites (green balls), 2 Al1 and 6 Al2 sites (red balls) and 6 O1 sites (blue balls), and ~50% occupied O2, O3A and O3B sites (blue-white double color balls). Partial occupancy of oxygen sites in this structure is physically reasonable because all oxygen sites showing 50% occupancy are contained in pairs with atomic separations that are too close to be physically reasonable (1.17 \AA apart for O2 and 0.88 \AA apart for O3A and O3B). Therefore, each pair should be considered as a unit representing at most a single oxygen atom located on only one of the two sites within each pair. Accordingly, a simplified structure model

is drawn in Figure 7b, showing only one oxygen atom for each O2, O3A and O3B pair at halfway positions (note that this model is only an approximation since the oxygen atoms at O2, O3A and O3B are actually located at one particular site of each pair). Further structural refinement with an improved fit to the measurements indicates additional vacancies located at 20% of the oxygen sites, resulting in 80% occupied O1 sites and 40% occupied O2, O3A and O3B sites (Table S3). The oxygen vacancies are physically expected since only 16 O anions are needed to form charge-balanced, stoichiometric (Sr_{0.89}Eu_{0.11})₄Al₈O₁₆ in this structure. Considering these observations, the chemical formula for the γ -SE_{0.11}AO unit cell could equivalently be represented as [(Sr_{0.89}Eu_{0.11})₄Al₈O₂₀]⁸⁺ + 4V_O, where the former denotes the lattice framework and the four oxygen vacancies (V_O) compensate the positive charge of the framework. This chemical formula provides a useful way to visualize the lattice structure and reproduces the composition (Sr_{0.89}Eu_{0.11}Al₂O₄), which is consistent with charge balance for Eu²⁺ ions as well as the composition measurement results. However, since oxygen scattering is relatively weak, the present scattering data is not sensitive to refinements attempting to further identify preferred sites for the oxygen vacancies.

The oxygen vacancies in the γ -SE_{0.11}AO crystal are partially ordered, as evidenced by the superstructure streaks observed in Laue microdiffraction pattern (Figure 6c), and are part of the average lattice structure. The partially ordered intrinsic oxygen vacancies are not common for the phosphors fabricated by conventional fabrication techniques, but they are reasonable for the new γ -SEAO nanoribbons formed in the oxygen-deficient, thermal evaporation-based fabrication process.²⁴ As the optical properties discussed below, the partially ordered oxygen vacancies likely change the local environment at particular Eu emission sites and thus are partially responsible for the unusual optical properties observed in γ -SEAOs.

Optical properties of SEAO nanoribbons

In visual observations (under the excitation of a 365 nm UV lamp) we have observed that the emission colors of *b*-SEAO and *g*-SEAO nanoribbons were independent of Eu concentrations, while the emission colors of γ -SEAO nanoribbons changed from green-yellow to orange-yellow when the Eu concentration was increased (Figure 1). These visual observations were verified by spectral measurements, as the normalized PL emission spectra shown in Figures 8a–c (the non-normalized PL emission spectra are shown in Figure S5; the PL excitation spectra for the three SEAOs are shown in Figure S6). Figure 8a shows the PL emission spectrum of *b*-SE_{0.11}AO nanoribbons under 360 nm excitation at room temperature. The blue emission peaks at ~420 nm (i.e., ~23800 cm⁻¹) and shows a full width at half maximum (FWHM) of ~1920 cm⁻¹, which is typical for normal Eu²⁺ 4*f*⁶5*d* → 4*f*⁷ emission in solids.²³ Other *b*-SEAO nanoribbons with different Eu concentrations (including the extreme case of *b*-EAO)²⁴ exhibit the same broadband emission spectra as the *b*-SE_{0.11}AO. Figure 8b shows the PL emission spectrum of *g*-SE_{0.11}AO nanoribbons under 360 nm excitation at room temperature. The green emission peaks at ~520 nm (i.e., ~19230 cm⁻¹) and

exhibits a large FWHM of $\sim 3100\text{ cm}^{-1}$; these values are very close to those reported from green $\text{SrAl}_2\text{O}_4:\text{Eu}^{2+}$ phosphors.^{23,34} Such broadband green emission was ascribed to the $4f^65d \rightarrow 4f^7$ transition of Eu^{2+} ions, and particularly attributed to the preferential orientation of the Eu^{2+} $5d$ orbital along the host cation chain (constructed by Sr^{2+} and Eu^{2+} ions) in the monoclinic lattice.³⁴ Increasing the Eu concentration in g -SEAOs results in slightly red-shifted emission bands; for example, the emission band is red-shifted by about 5 nm from $g\text{-SE}_{0.11}\text{AO}$ to the extreme case of $g\text{-EAO}$ (Figure 8b). For all the b -SEAO and g -SEAO nanoribbons, the emission spectra at room temperature are independent of the excitation wavelengths.

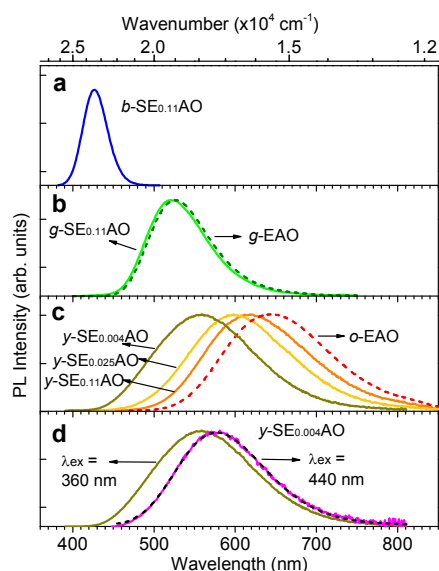


Figure 8. (a) PL emission spectrum of $b\text{-SE}_{0.11}\text{AO}$ nanoribbons under 360 nm excitation at room temperature. (b) PL emission spectrum of $g\text{-SE}_{0.11}\text{AO}$ nanoribbons under 360 nm excitation at room temperature (solid-line curve). The emission spectrum of $g\text{-EAO}$ (dashed-line curve) is also given for comparison. (c) PL emission spectra of $y\text{-SE}_{0.004}\text{AO}$, $y\text{-SE}_{0.025}\text{AO}$ and $y\text{-SE}_{0.11}\text{AO}$ nanoribbons under 360 nm excitation at room temperature (solid-line curves). The emission spectrum of $o\text{-EAO}$ (dashed-line curve) is also given for comparison. (d) PL emission spectra of $y\text{-SE}_{0.004}\text{AO}$ nanoribbons under 360 nm and 440 nm light excitation at room temperature (solid-line curves). The spectrum obtained under 360 nm excitation is the same as the one in (c). Both spectra are normalized by their maxima. The dashed-line curve is the Gaussian fit of the spectrum under 440 nm light excitation.

The solid curves in Figure 8c show the emission spectra of $y\text{-SE}_{0.004}\text{AO}$, $y\text{-SE}_{0.025}\text{AO}$ and $y\text{-SE}_{0.11}\text{AO}$ nanoribbons under 360 nm excitation at room temperature. It is clear that the emission bands of $y\text{-SE}_{0.004}\text{AO}$ (peaking at $\sim 560\text{ nm}$, i.e., $\sim 17850\text{ cm}^{-1}$; FWHM, $\sim 3719\text{ cm}^{-1}$), $y\text{-SE}_{0.025}\text{AO}$ (peaking at $\sim 600\text{ nm}$, i.e., $\sim 16670\text{ cm}^{-1}$; FWHM, $\sim 3826\text{ cm}^{-1}$), and $y\text{-SE}_{0.11}\text{AO}$ (peaking at $\sim 620\text{ nm}$, i.e., $\sim 16130\text{ cm}^{-1}$; FWHM, $\sim 3921\text{ cm}^{-1}$) shift to longer-wavelengths when the Eu molar fraction in y -SEAOs is increased from 0.004 to 0.11. These spectral results are in good agreement with the visual observation shown in Figures 1e–g. A further increase of the Eu concentration

results in more red-shifted emission bands until reaching the extreme case of $o\text{-EAO}$ whose emission band peaks at $\sim 645\text{ nm}$ (i.e., 15500 cm^{-1}) with a FWHM of $\sim 3640\text{ cm}^{-1}$,²⁴ as the dashed-line curve shown in Figure 8c. It is worth noting that the FWHM values of the yellow emissions in y -SEAOs are the largest ever observed in Eu^{2+} -activated aluminate-based materials.²³ At the other extreme end where Eu is completely eliminated, the resulting strontium aluminate products do not emit any light. The emission red-shift in g -SEAOs and y -SEAOs with the increase of Eu concentration were previously observed in some other Eu^{2+} -activated luminescent materials.^{39–41} Although the possible reasons for such red-shift can be the re-absorption and energy transfer between different Eu^{2+} sites (energy transfer between two Eu^{2+} sites does exist in y -SEAOs as will be discussed later),^{39–41} we believe that the emission red-shift is also probably associated with the intrinsic oxygen vacancies in the crystal lattices. Since oxygen vacancies require some electron density to gain stability, the Eu^{2+} ions partially delocalize their d electrons toward these oxygen vacancies. The electron delocalization thus reduces the average radius of the host Eu cations. As a result, the crystal-field strength around the Eu emitting centers is increased, leading to enhanced crystal-field splitting of the $4f^65d$ configuration. With the increase of Eu concentration in the materials, the average radius of the cations tends to decrease, resulting in the increase of crystal-field strength and thus the red-shift of the emission.

It is also noted that while the emission bands of $y\text{-SE}_{0.025}\text{AO}$ and $y\text{-SE}_{0.11}\text{AO}$ are independent of the excitation wavelengths, the emission band of $y\text{-SE}_{0.004}\text{AO}$ is excitation wavelength-dependent. For example, as shown in Figure 8d, the emission band of $y\text{-SE}_{0.004}\text{AO}$ produced under 360 nm light excitation is asymmetric on an energy scale with the peak located at $\sim 560\text{ nm}$ (i.e., $\sim 17850\text{ cm}^{-1}$), while excitation with 440 nm light produces a single Gaussian band peaking at $\sim 580\text{ nm}$ (i.e., 17240 cm^{-1}). As will be discussed later, this excitation wavelength-dependent emission suggests that probably more than one Eu^{2+} luminescence sites contribute to the emission in $y\text{-SE}_{0.004}\text{AO}$ at room temperature.

We also measured the PL emission and excitation spectra of y -SEAOs at 77 K. In contrast to the room temperature luminescence, at 77 K the emission and excitation spectra of all y -SEAOs are dependent on their respective excitation and monitoring wavelengths, as the spectra shown in Figures 9a–c. The emission bands acquired under 360 nm excitation are asymmetric, and each of them can be fit by two Gaussian bands, as shown by the dashed-line curves in Figures 9a–c. Excitation with 440 nm light produces single Gaussian emission bands, which perfectly overlap the low-energy Gaussian fitting bands for the emission bands produced by 360 nm excitation. These results clearly indicate that there exist two different Eu^{2+} luminescent sites with different emitting energy in the hexagonal y -SEAOs at 77 K. We call them Eu_1 site and Eu_2 sites, corresponding to the low-energy site and high-energy site, respectively. It is apparent from Figures 9a–c that at 77 K the high-energy 360 nm light can excite emissions from both Eu_1 and Eu_2 sites, while the low-energy 440 nm light can only excite the low-energy Eu_1 emission.

To understand the emitting nature of the two Eu^{2+} sites in y -SEAO nanoribbons, we measured wavelength dependent

luminescence decays under the excitation of a 355 nm pulsed laser at 77 K. Figures 9d and 9e show, respectively, the emission decay curves of γ -SE_{0.025}AO and γ -SE_{0.004}AO at 700 nm (involving only Eu₁ sites) and 520 nm (dominated by Eu₂ sites). In γ -SE_{0.025}AO (Figure 9d), the decay curve of the 700 nm emission exhibits an initial build-up process (inset of Figure 9d) followed by a single exponential decay behavior with a fitted lifetime of 1.22 μ s, while the decay curve of the 520 nm emission is multi-exponential and shows a much faster initial decay process than that of the 700 nm emission. The build-up process in the 700 nm emission and the initial faster decay process in the 520 nm emission indicate that an energy transfer from Eu₂ site to Eu₁ site occurs in γ -SE_{0.025}AO.^{42,43} In contrast, the emission at 700 nm and 520 nm from γ -SE_{0.004}AO show similar decay process at the initial stage (inset of Figure 9e); each emission exhibits a single exponential decay curve with a fitted lifetime of 1.15 μ s for the 700 nm emission and 0.89 μ s for the 520 nm emission, indicating that there is no energy transfer between Eu₂ and Eu₁ sites in γ -SE_{0.004}AO at 77 K.

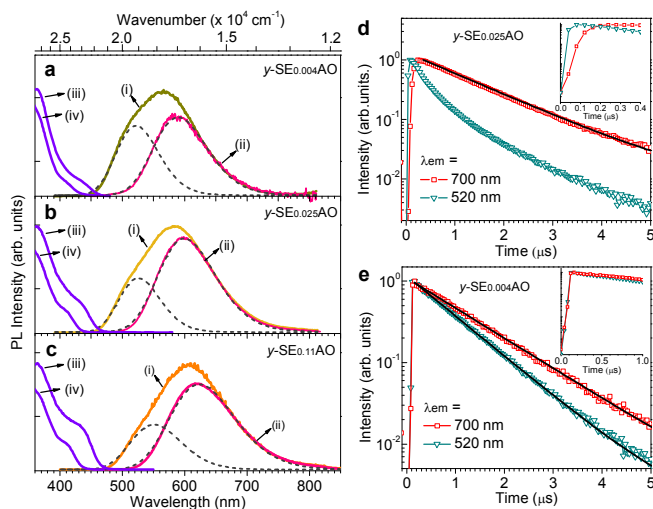


Figure 9. (a–c) PL emission and excitation spectra of γ -SE_{0.004}AO, γ -SE_{0.025}AO and γ -SE_{0.11}AO nanoribbons at 77 K. In each panel, solid-line curve (i) is the emission spectrum acquired under 360 nm excitation; solid-line curve (ii) is the emission spectrum acquired under 440 nm excitation; solid-line curve (iii) is the excitation spectrum by monitoring at 700 nm emission; solid-line curve (iv) is the excitation spectrum by monitoring at 520 nm emission; and dashed-line curves are the Gaussian fit of spectra (i). (d) Luminescence decay curves of γ -SE_{0.025}AO monitored at 520 nm (open triangle) and 700 nm (open square) at 77 K. The black solid line is the fitted profile of the decay curve monitored at 700 nm emission. Inset is an enlarged view of the initial stages of the decays for the two emission wavelengths. (e) Luminescence decay curves of γ -SE_{0.004}AO monitored at 520 nm (open triangle) and 700 nm (open square) at 77 K. The black solid lines are the fitted profiles. Inset is an enlarged view of the initial stages of the decays for the two emission wavelengths.

It is generally accepted that the probability of energy transfer between two emission sites in a phosphor is inversely proportional to the distance between the two sites.^{44,45} This is true for the γ -SEAOs with different Eu concentrations. The distance between the two Eu²⁺ emission sites in low-Eu containing γ -SEAOs, e.g., γ -SE_{0.004}AO, is

certainly larger than that in the higher-Eu containing γ -SEAOs, e.g., γ -SE_{0.025}AO; thus, the probability of energy transfer between the Eu²⁺ emission sites in γ -SE_{0.025}AO is higher than that in γ -SE_{0.004}AO. Therefore, at room temperature, both Eu₁ and Eu₂ sites in γ -SE_{0.004}AO emit light under 360 nm light excitation, resulting in an asymmetric emission band (Figure 8c) and a green-yellow emission color (Figure 1g). In γ -SE_{0.025}AO and γ -SE_{0.11}AO, in contrast, the site-to-site energy transfer nearly quenches the emission from the Eu₂ site at room temperature, leading to a single Gaussian band from the Eu₁ site (Figure 8c).⁴⁵ At 77 K, the energy transfer between the two Eu²⁺ sites is partially suppressed by a reduction in the phonon-assisted energy transfer due to the shift of the available phonon distribution to lower phonon energies. This results in the appearance of the Eu₂ emission band in γ -SE_{0.025}AO and γ -SE_{0.11}AO under 360 nm light excitation and thus the excitation wavelength-dependent emission (Figures 9b and 9c).

The above spectral investigations provide clear evidences for the existence of two different Eu²⁺ luminescent sites in γ -SEAOs. Since the ligand arrangements around all Eu²⁺ ions are the same in the original [(Sr_{0.89}Eu_{0.11})₄Al₈O₂₀]⁸⁻ unit cell (Figure 7), the presence of the two kinds of Eu²⁺ luminescent sites in the charge-balanced unit cell likely originates from the partially ordered oxygen vacancies in the materials. That is, the partial ordering of oxygen vacancies can modulate the crystal field environments around different Eu²⁺ ions, making some Eu²⁺ ions close to the oxygen vacancies and some not. This would lead to the formation of two kinds of non-equivalent Eu²⁺ luminescent sites, i.e., Eu₁ site and Eu₂ site, in the lattice.

Moreover, luminescence quantum efficiency measurements showed that the quantum efficiencies of the SEAO nanoribbons are general good, with measured values for the *b*-, *g*-, and γ -SE_{0.11}AO nanoribbons are ~20%, ~32%, and ~36%, respectively, under 360 nm excitation at room temperature. The luminescence stability of the SEAO nanoribbons is outstanding; almost no luminescence degradation was observed after the nanoribbons were left in ambient environment for one year.

SEAO nanoribbon waveguides

The above results show that the three series of SEAO luminescent nanoribbons exhibit broadband blue, green and tunable yellow emissions (from green-yellow to yellow, and to orange-yellow) originating from Eu²⁺ luminescence centers. These new luminescent nanoribbons are expected to act as both light generators and waveguides in nanoscale photonic devices. We became aware of such potential when we were performing Laue microdiffraction measurements.

Figures 10a–d show optical micrographs of individual *b*-SE_{0.025}AO, *g*-SE_{0.025}AO, γ -SE_{0.025}AO, and γ -SE_{0.004}AO nanoribbons being struck by a focused X-ray microbeam (~0.5 μ m diameter). Strong visible emission exhibiting the color of the respective type of SEAOs is generated locally at the position where the X-ray beam strikes the individual ribbon. The luminescence colors and emission spectra (Figure S7) under X-ray excitation are consistent with those excited by UV light. The generated light propagates, up to several hundreds of micrometers, along the ribbons and emanates at their ends

(indicated by white arrows in Figures 10a–d). Besides emanating at the ribbon's ends, light is also scattered in a series of spots along the *g*-SE_{0.025}AO (Figure 10b) and *y*-SE_{0.025}AO (Figure 10c) ribbons, probably due to the presence of local non-uniformities (e.g. surface steps or roughness) along the ribbon.⁵ In addition to propagating within an individual ribbon, the generated light in one ribbon can also be routed to another ribbon by contact. Figure 10d shows that the green-yellow light generated in a long *y*-SE_{0.004}AO ribbon is routed to a staggered short ribbon (the junction is indicated by a white dashed-line arrow) and emanates at its end. It is apparent that the junction of the two staggered ribbons acts as both the scattering center and the source of the light propagating along the short ribbon. The same light generation, propagation and routing phenomenon is also observed from *b*-SE_{0.025}AO ribbons, as shown in Figure 10e. The light routing observed among ribbons suggests that in an optical network constructed using different SEAO ribbons, it is possible to achieve simultaneous generation, propagation and routing of blue, green, and yellow light in an optical device.

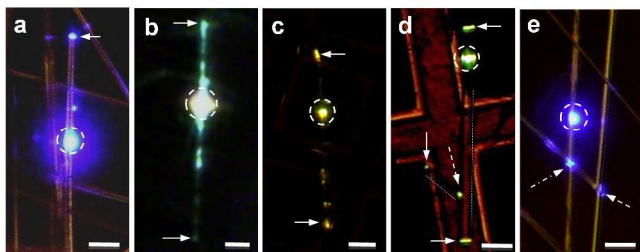


Figure 10. (a–c) Optical micrograph showing the generation and propagation of light in individual *b*-SE_{0.025}AO, *g*-SE_{0.025}AO and *y*-SE_{0.025}AO nanoribbons when the ribbons are struck by a focused X-ray microbeam (~0.5 μm in diameter). (d) Optical micrograph of two staggered *y*-SE_{0.004}AO nanoribbons with the longer one being struck by a focused X-ray microbeam. The orientations of the two ribbons are indicated by dashed lines. (e) Optical micrograph of several staggered *b*-SE_{0.025}AO nanoribbons with one ribbon being struck by a focused X-ray microbeam. The dashed-line circles in (a–e) indicate the X-ray beam positions. The solid arrows in (a–d) indicate light emanating at the ends of the ribbons. The dashed arrows in (d, e) indicate the junctions where the light is routed from one ribbon to the one lying on it. The scale bars are 20 μm.

Conclusions

In summary, by using a carbothermal reaction and vapor-phase deposition method, we have synthesized three series of Eu²⁺-activated quaternary strontium europium aluminate (SEAOs) luminescent nanoribbons, i.e., blue luminescent, tetragonal Sr_{1-x}Eu_xAl₆O₁₀ (0 < x < 1), green luminescent, monoclinic Sr_{1-x}Eu_xAl₂O₄ (0 < x < 1), and yellow luminescent, hexagonal Sr_{1-x}Eu_xAl₂O₄ (0 < x < 1). Among these three series of SEAO nanoribbons, the *b*-SEAOs and *y*-SEAOs are new compounds that have not been reported before. While the emission wavelengths of *b*-SEAOs and *g*-SEAOs are independent of Eu concentrations, the *y*-SEAOs shows tunable

emission colors from green-yellow to orange-yellow when the Eu concentration is increased. Moreover, synchrotron X-ray microdiffraction measurements showed that there exist partially ordered oxygen vacancies in *y*-SEAO lattices, which are likely responsible for the unusual optical properties observed in *y*-SEAOs. These new SEAO luminescent nanoribbons can function as both light generators and waveguides, and thus have promising potential as the building blocks in future miniaturized photonic circuitry.

Acknowledgements

Z.W.P. acknowledges the funding support from the US National Science Foundation (NSF, DMR-0955908). J.D.B. was supported by the Materials Sciences and Engineering Division, Office of Basic Energy Sciences (BES), U.S. Department of Energy (DOE). Use of the APS beamlines 34-ID-E and 11-BM-B (by J.D.B. and J.Z.T.), ChemMatCARS Sector 15 (by Y.S.C. and J.D.B.) and 20-BM-B (by C.J.S.) were supported by U.S. DOE under Contract No. DE-AC02-06CH11357 with Argonne National Laboratory. ChemMatCARS Sector 15 is principally supported by the Divisions of Chemistry and Materials Research, NSF, under grant number NSF/CHE-1346572. The TEM characterization (by J.Y.H.) was conducted at the Oak Ridge National Laboratory ShaRE User Facilities, which is sponsored by the Division of Scientific User Facilities of BES, U.S. DOE.

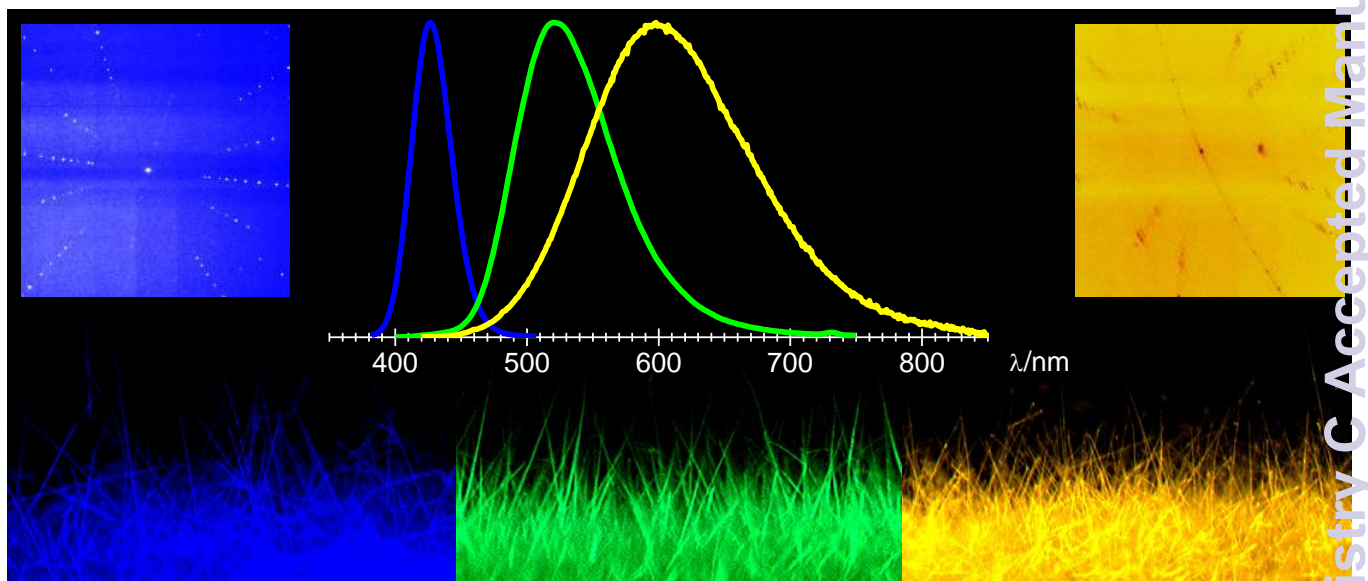
Notes and references

- ^a College of Engineering and ^b Department of Physics and Astronomy, University of Georgia, Athens, Georgia 30602, U.S.A.
^c Materials Science and Technology Division, Oak Ridge National Laboratory, Oak Ridge, Tennessee 37831, U.S.A.
^d ChemMatCARS, University of Chicago, Argonne, Illinois 60439, U.S.A.
^e X-ray Science Division, Argonne National Laboratory, Argonne, Illinois 60439, U.S.A.
^f Advanced Photon Source, Argonne National Laboratory, Argonne, Illinois 60439, U.S.A.
[§] Present address: Center for Nanophase Materials Sciences, Oak Ridge National Laboratory, Oak Ridge, Tennessee 37831, USA.
[‡] Present address: Hitachi High-Technologies Canada Inc., 89 Galaxy Blvd, Suite 14, Toronto, ON M9W 6A4, Canada.
* Corresponding authors, E-mails: panz@uga.edu, budajjd@ornl.gov
† Electronic Supplementary Information (ESI) available: Figures of experimental set-up, XANES spectra, synchrotron powder XRD patterns, unit cell structures, PL excitation spectra, and X-ray excited PL spectra. Tables of JADE fitting of synchrotron powder XRD patterns and atomic coordinates. See DOI: 10.1039/b000000x/

- 1 R. X. Yan, D. Gargas and P. D. Yang, *Nat. Photonics* **2009**, *3*, 569.
- 2 P. J. Pauzauskie and P. D. Yang, *Mater. Today* **2006**, *9*, 36.
- 3 C. J. Barrelet, A. B. Greytak and C. M. Lieber, *Nano Lett.* **2004**, *4*, 1981.
- 4 A. Mekis, J. C. Chen, I. Kurland, S. H. Fan, P. R. Villeneuve and J. D. Joannopoulos, *Phys. Rev. Lett.* **1996**, *77*, 3787.

- 5 M. Law, D. J. Sirbuly, J. C. Johnson, J. Goldberger, R. J. Saykally and P. D. Yang, *Science* **2004**, *305*, 1269.
- 6 D. J. Sirbuly, M. Law, P. Pauzauskie, H. Q. Yan, A. V. Maslov, K. Knutsen, C. –Z. Ning, R. J. Saykally and P. D. Yang, *Proc. Natl. Acad. Sci.* **2005**, *102*, 7800.
- 7 M. H. Huang, S. Mao, H. Feick, H. Q. Yan, Y. Y. Wu, H. Kind, E. Weber, R. Russo and P. D. Yang, *Science* **2001**, *292*, 1897.
- 8 X. F. Duan, Y. Huang, R. Agarwal and C. M. Lieber, *Nature* **2003**, *421*, 241.
- 9 H. Q. Yan, J. Johnson, M. Law, R. R. He, K. Knutsen, R. McKinney, J. Pham, R. Saykally and P. D. Yang, *Adv. Mater.* **2003**, *15*, 1907.
- 10 F. Qian, Y. Li, S. Gradečak, D. L. Wang, C. J. Barrelet and C. M. Lieber, *Nano Lett.* **2004**, *4*, 1975.
- 11 F. Qian, S. Gradečak, Y. Li, C. –Y. Wen and C. M. Lieber, *Nano Lett.* **2005**, *5*, 2287.
- 12 Y. Huang, X. F. Duan and C. M. Lieber, *Small* **2005**, *1*, 142.
- 13 J. F. Wang, M. S. Gudiksen, X. F. Duan, Y. Cui and C. M. Lieber, *Science* **2001**, *293*, 1455.
- 14 Y. Nakayama, P. J. Pauzauskie, A. Radenovic, R. M. Onorato, R. J. Saykally, J. Liphardt and P. D. Yang, *Nature* **2007**, *447*, 1098.
- 15 D. Psaltis, *Science* **2002**, *298*, 1359.
- 16 A. B. Djurišić and Y. H. Leung, *Small* **2006**, *2*, 944.
- 17 J. Q., Hu, X. L. Ma, N. G. Shang, Z. Y. Xie, N. B. Wong, C. S. Lee and S. T. Lee, *J. Phys. Chem. B* **2002**, *106*, 3823.
- 18 B. Cheng, J. M. Russell, W. S. Shi, L. Zhang and E. T. Samulski, *J. Am. Chem. Soc.* **2004**, *126*, 5972.
- 19 G. Blasse, and B. C. Grabnaier, *Luminescent Materials*. **1994**, Springer-Verlag, Berlin.
- 20 G. Blasse and A. Bril, *Philips Res. Rep.* **1968**, *23*, 201.
- 21 G. Blasse, W. L. Wanmaker and J. W. ter Vrugt, *J. Electrochem. Soc.* **1968**, *115*, 673.
- 22 C. Duan, X. Wu, W. Li, H. Chen, X. Feng and J. Zhan, *Appl. Phys. Lett.* **2005**, *87*, 201917.
- 23 P. Dorenbos, *J. Lumin.* **2003**, *104*, 239.
- 24 F. Liu, J. D. Budai, X. F. Li, J. Z. Tischler, J. Y. Howe, C. J. Sun, R. S. Meltzer and Z. W. Pan, *Adv. Funct. Mater.* **2013**, *23*, 1998.
- 25 G. Schierning, M. Batenschuk, A. Osvet, A. Stiegelschmitt and A. Winnacker, *Phys. Stat. Sol. (c)* **2005**, *2*, 109.
- 26 J. S. Becker, *Spectrochim. Acta B* **2002**, *57*, 1805.
- 27 S. M. Heald, D. L. Brewster, E. A. Stern, K. H. Kim, F. C. Brown, D. T. Jiang, E. D. Crozier and R. A. Gordon, *J. Synchrotron Rad.* **1999**, *6*, 347–349.
- 28 J. Wang, B. H. Toby, P. L. Lee, L. Ribaud, S. M. Antao, C. Kurtz, M. Ramanathan, R. B. Von Dreele and M. A. Beno, *Rev. Sci. Instrum.* **2008**, *79*, 085105.
- 29 B. C. Larson, W. G. Yang, G. E. Ice, J. D. Budai and J. Z. Tischler, *Nature* **2002**, *415*, 887.
- 30 J. D. Budai, W. G. Yang, N. Tamura, J. –S. Chung, J. Z. Tischler, B. C. Larson, G. E. Ice, C. Park and D. P. Norton, *Nat. Mater.* **2003**, *2*, 487.
- 31 Z. W. Pan, J. D. Budai, Z. R. Dai, W. J. Liu, M. P. Paranthaman and S. Dai, *Adv. Mater.* **2009**, *21*, 890.
- 32 G. E. Ice, J. D. Budai and J. W. L. Pang, *Science*, **2011**, *334*, 1234.
- 33 V. Abbruscato, *J. Electrochem. Soc.* **1971**, *118*, 930.
- 34 S. H. M. Poort, W. P. Blokpoel and G. Blasse, *Chem. Mater.* **1995**, *7*, 1547.
- 35 Z. Tang, F. Zhang, Z. Zhang, C. Huang and Y. Lin, *J. Eur. Ceram. Soc.* **2000**, *20*, 2129.
- 36 N. Y. Yu, F. Liu, X. F. Li and Z. W. Pan, *Appl. Phys. Lett.* **2009**, *95*, 231110.
- 37 K. Kato, I. Tsutai, T. Kamimura, F. Kaneko, K. Shinbo, M. Ohta and T. Kawakami, *J. Lumin.* **1999**, *82*, 213.
- 38 C. D. Ling, R. L. Withers, S. Schmid and J. G. Thompson, *J. Solid State Chem.* **1998**, *137*, 42.
- 39 V. Bachmann, C. Ronda, O. Oeckler, W. Schnick, A. Meijerink, *Chem. Mater.* **2009**, *21*, 316.
- 40 Y. Q. Li, A. C. A. Delsing, G. de With and H. T. Hintzen, *Chem. Mater.* **2005**, *17*, 3242.
- 41 Y. Q. Li, J. E. J. van Steen, J. W. H. van Krevel, G. Botty, A. C. A. Delsing, F. J. DiSalvo, G. de With and H. T. Hintzen, *J. Alloys Compd.* **2006**, *417*, 273.
- 42 A. A. Setlur, W. J. Heward, M. E. Hannah and U. Happek, *Chem. Mater.* **2008**, *20*, 6277.
- 43 Y. F. Liu, X. Zhang, Z. D. Hao, X. J. Wang and J. H. Zhang, *J. Mater. Chem.* **2011**, *21*, 6354.
- 44 M. J. Weber, *Phys. Rev. B* **1971**, *4*, 2932.
- 45 S. J. Lee and K. –S. Sohn, *Opt. Lett.* **2010**, *35*, 1004.

Table of Contents



We report the synthesis, crystal structure characterization and optical properties of three series of new quaternary strontium europium aluminate luminescent nanoribbons with luminescence colors of blue, green and yellow.